2021

Modulation of spin-orbit torque from SrRuO3 by epitaxial-strain-induced octahedral rotation

J. Zhou, X. Shu, W. Lin, D. F. Shao, S. Chen, L. Liu, P. Yang, E. Y. Tsymbal, and J. Chen

Modulation of Spin–Orbit Torque from SrRuO₃ by Epitaxial-Strain-Induced Octahedral Rotation

Jing Zhou, Xinyu Shu, Weinan Lin, Ding Fu Shao, Shaohai Chen, Liang Liu, Ping Yang, Evgeny Y. Tsymbal, and Jingsheng Chen*

Spin–orbit torque (SOT), which arises from the spin–orbit coupling of conduction electrons, is believed to be the key route for developing low-power, high-speed, and nonvolatile memory devices. Despite the theoretical prediction of pronounced Berry phase curvatures in certain transition-metal perovskite oxides, which lead to considerable intrinsic spin Hall conductivity, SOT from this class of materials has rarely been reported until recently. Here, the SOT generated by epitaxial SrRuO₃ of three different crystal structures is systematically studied. The results of both spin-torque ferromagnetic resonance and in-plane harmonic Hall voltage measurements concurrently reveal that the intrinsic SOT efficiency of SrRuO₃ decreases when the epitaxial strain changes from tensile to compressive. The X-ray diffraction data demonstrate a strong correlation between the magnitude of SOT and octahedral rotation around the in-plane axes of SrRuO₃, consistent with the theoretical prediction. This work offers new possibilities of tuning SOT with crystal structures and novel opportunities of integrating the unique properties of perovskite oxides with spintronic functionalities.

Current induced spin–orbit torque (SOT), which arises from the spin–orbit coupling between the electron spin and the orbital angular momentum, has proved to be a subject of strong academic interest and a promising scheme for developing low-power magnetic devices.[1–3] Traditionally, materials generating a large SOT are predominantly semiconductors[4,5] and heavy metals.[3,6,7] Other SOT materials have also been investigated, such as antiferromagnets,[8,9] topological insulators,[10,11] and 2D materials.[12–14] Oxides, which have poor electrical conductivity in general, have remained naturally unexplored in the discipline of SOT until recently. Certain 4d and 5d transition metal oxides, such as SrIrO₃ and SrRuO₃, exhibit moderate electrical conductivity and strong Berry phase curvatures,[15–17] which give rise to large intrinsic spin Hall conductivity (SHC). Therefore, these oxides are potentially good sourcing materials for SOT.

The transition metal oxides have a multitude of degrees of freedom, such as the crystal lattice, charge, spin, and orbital. These tunable parameters are interconnected with each other and are not always fully accessible in other material classes. The perovskite crystal structure of SrRuO₃ has been extensively studied since the rotation of the RuO₆ octahedra has enormous impacts on its electrical and magnetic properties.[18–26] This octahedral rotation is expected to influence SOT as well from two perspectives. First, the band structure of SrRuO₃ determines its intrinsic SHC, which is strongly influenced by the octahedral crystal field.[27–30] Second, the octahedral rotation may alter the local inversion symmetry, which has been demonstrated to be crucial for SOT generation.[12,31,32] Therefore, tuning the octahedral rotation represents a distinguished means of modulating SOT since it potentially allows external control of the intrinsic SHC. For instance, it has been demonstrated in a variety of perovskite oxides that the octahedral rotation can be controlled by an electric field.[33–35] This offers greater flexibility in designing full-electric-field-controlled SOT memory devices. In recent studies, sizable SOT has been observed experimentally in both SrIrO₃ and SrRuO₃.[36–38] Variations of the SOT efficiency with the thickness of SrIrO₃ and SrRuO₃ were attributed to the thickness-dependent octahedral rotation.[36,38] However, the relation between the octahedral rotation and SOT is still blurred due to limited evidences.

In this work, we investigate the effects of the octahedral rotation on the SOT generated by SrRuO₃ above its Curie temperature. By carefully engineering the epitaxial strain, we deposit three types of SrRuO₃ thin films with different octahedral rotations. We examine the SOT in SrRuO₃/Ni₈₁Fe₁₉ [also referred as Permalloy (Py)] bilayer using both spin-torque ferromagnetic resonance (ST-FMR) and in-plane harmonic Hall voltage (HHV) techniques. The results from the two techniques agree

Dr. J. Zhou, X. Shu, Dr. W. Lin, Dr. S. Chen, Dr. L. Liu, Dr. P. Yang, Prof. J. Chen
Materials Science and Engineering
National University of Singapore
9 Engineering Drive 1, Singapore 117575, Singapore
E-mail: msecj@nus.edu.sg
Dr. D. F. Shao, Prof. E. Y. Tsymbal
Department of Physics and Astronomy and Nebraska Center for Materials and Nanoscience
University of Nebraska
Lincoln, NE 68588, USA
Dr. P. Yang
Singapore Synchrotron Light Source (SSLS)
National University of Singapore
5 Research Link, Singapore 117603, Singapore

**ADVANCED
SCIENCE NEWS**

www.advancedsciencenews.com

**ADVANCED
MATERIALS**

www.advmat.de

with each other. Relatively larger SOT efficiencies are observed in SrRuO₃ thin films under a large tensile strain or a small compressive strain, which correspond to octahedral rotations around the in-plane axes of SrRuO₃. By contrast, such octahedral rotations are absent for SrRuO₃ thin films under a large compressive strain, where negligible SOT is generated. Furthermore, we find that the SOT efficiencies of SrRuO₃ decrease rapidly with increasing temperature (decreasing electrical conductivity). This suggests the dominant contribution to SOT in SrRuO₃ is the intrinsic SHC in the "dirty metal" regime[36,39] and therefore supports the influence of the octahedral rotation.

Bilayers of SrRuO₃ (10, 20 nm)/Py(4 nm) are prepared using pulsed laser deposition and DC magnetron sputtering (see the Experimental Section). Taking into account the lattice mismatch with bulk SrRuO₃, we choose three different single-crystal substrates, namely, NdGaO₃ (001)ₑ (the "c" in the subscript denotes pseudocubic lattice), SrTiO₃ (001) and KTaO₃ (001) (hereby referred as NGO, STO, and KTO). Their bulk lattice constants (a) take the following order: $a_{NGO} < a_{STO} < a_{SrRuO_3} < a_{KTO}$. In our previous reports,[18,40] we found that the large compressive strain from NGO enhances (suppresses) the octahedral rotation about the out-of-plane (in-plane) axis of SrRuO₃. By contrast, a large tensile strain from KTO stretches the network of octahedra and induces substantial octahedral rotation around the in-plane axes of SrRuO₃. In the case of STO, a small compressive strain results in an intermediate structure between the two extremes. **Figure 1**a schematically illustrates the effects of epitaxial strain on the lattice parameters of SrRuO₃.

We first examine the crystal structures of the epitaxial SrRuO₃ thin films using X-ray diffraction (XRD). The $\theta - 2\theta$ scans that probe along the [00L] direction in reciprocal space

are shown in Figure 1b. For all three curves, all peaks from the {001}ₑ family of the bulk SrRuO₃ crystal but no other film peaks are observed in the diffraction pattern. This indicates good crystallinity and (001)ₑ epitaxy of the SrRuO₃ films on all substrates. The inset shows an enlarged view of a representative (002)ₑ film peak with Laue oscillation, which further confirms the high crystallinity. Two tests are performed to verify the epitaxial relations in the film plane. Figure 1c shows a typical ϕ-scan. Both the substrates and the film exhibit a fourfold symmetry of the 103 peak indicating only a negligible phase difference between the substrate and the film peaks. This suggests that the epitaxial relation of substrate/SrRuO₃ is [100]/[100]ₑ. The typical reciprocal space mappings (RSMs) around (103) are shown in Figure 1d. For all three substrates, the film and substrate have similar H values. This verifies the epitaxial relation derived by the ϕ-scan and also suggests that our SrRuO₃ films are almost fully strained. Based on the reciprocal space vectors,[41] we extract the lattice constants of SrRuO₃ as follows: $a = b = 3.989$ Å and $c = 3.898$ Å for KTO/SrRuO₃; $a = 3.917$ Å, $b = 3.933$ Å and $c = 3.946$ Å for STO/SrRuO₃; $a = b = 3.850$ Å and $c = 4.013$ Å for NGO/SrRuO₃. All angles between the unit cell sides are measured to be 90° within experimental error, except β for SrRuO₃ on STO, which is 89.6°, as indicated in Figure 1a. It is worth noting that lattice parameters alone are insufficient to determine the structural phase of SrRuO₃ when an octahedral rotation is present, since the octahedral rotation can lower the symmetry derived from lattice parameters.

The SOT in the SrRuO₃/Py bilayers is evaluated using the ST-FMR technique at room temperature[3,9,31] (see the Experimental Section; Note S1 of the Supporting Information for details). **Figure 2**a shows the schematic setup, where
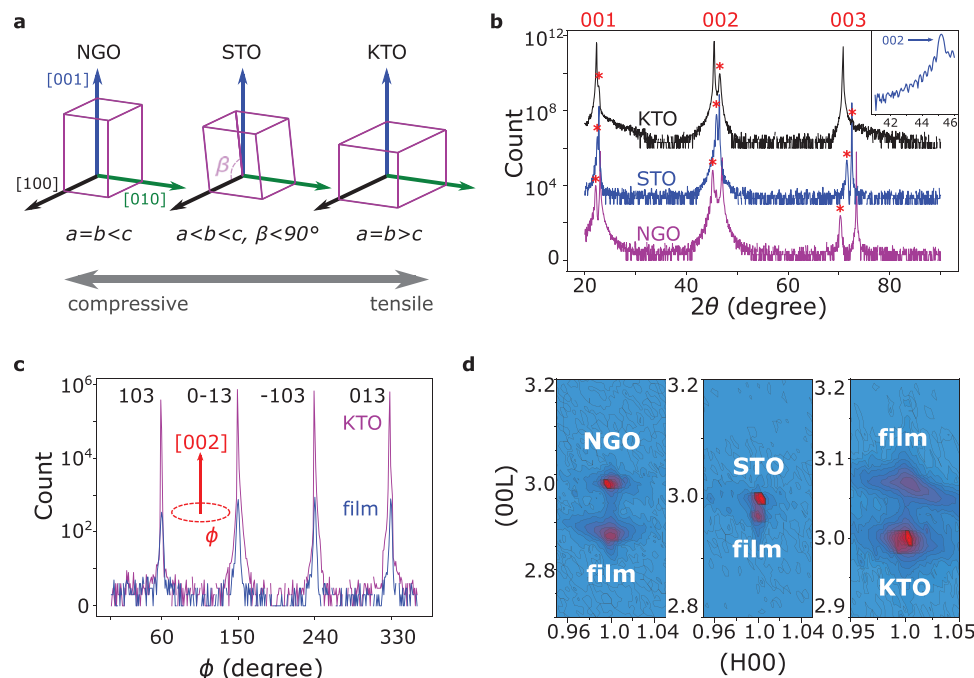

Figure 1. Epitaxial growth of SrRuO₃ thin films. a) Schematic illustration of the effects of epitaxial strain on the lattice parameters of SrRuO₃. The coordinates are labeled as mutually orthogonal in pseudocubic lattice. b) $\theta - 2\theta$ scans that probe along [00L] direction in reciprocal space. Film peaks are labelled with "*". The inset shows an enlarged picture of 002 peak of SrRuO₃ on STO. Arbitrary back grounds are added separate the plots. c) ϕ scan of KTO/SrRuO₃. d) RSMs around (103) of SrRuO₃ films on different substrates.
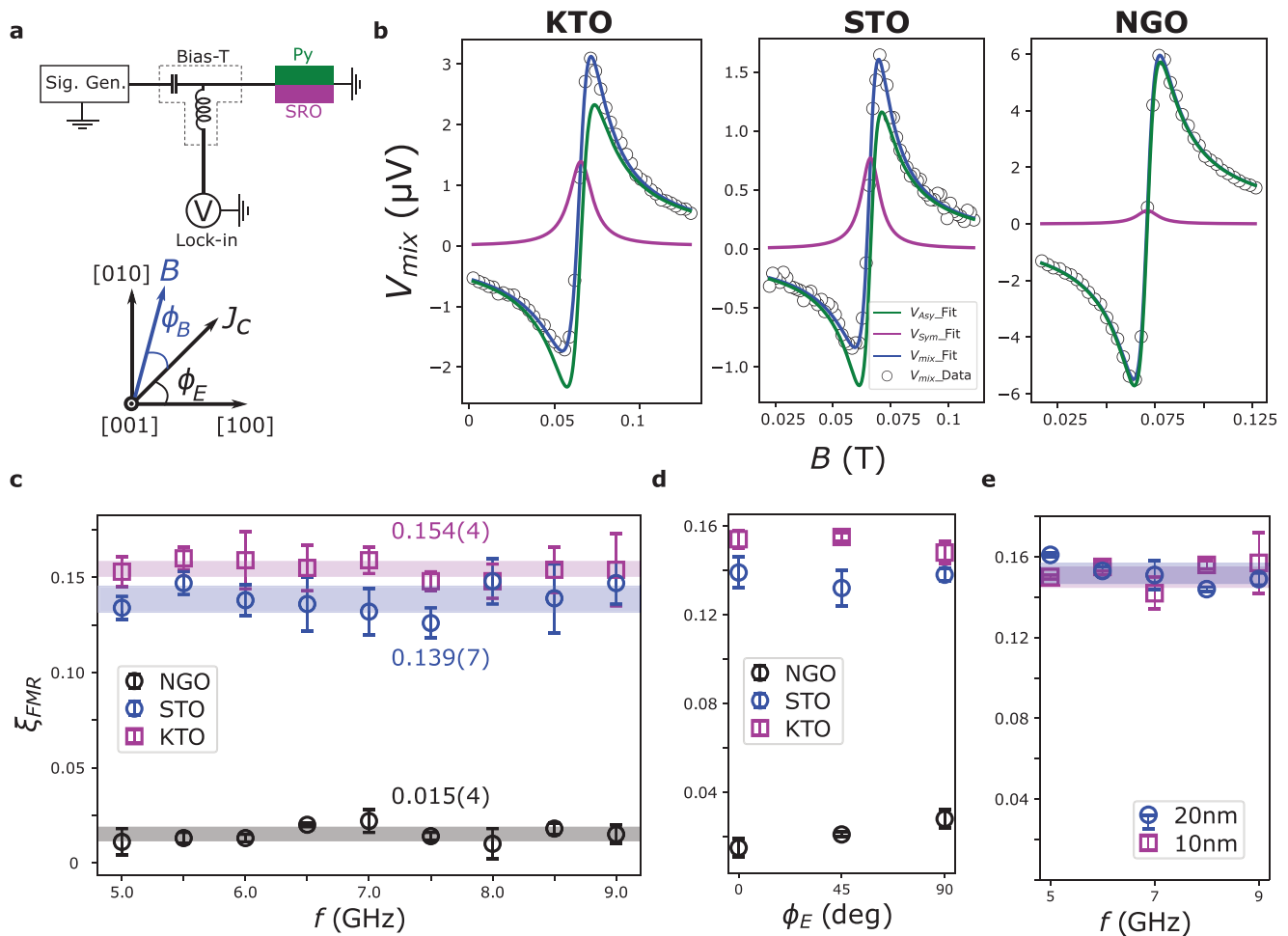
Figure 2. SOT efficiency (ξ_{FMR}) measured by ST-FMR. a) Schematic setup. The coordinate system is based on the crystal lattice of the SrRuO$_3$ film. b) Measured ST-FMR voltage (V_{mix}) at 7 GHz from SrRuO$_3$ (20 nm)/Py (4 nm) bilayer deposited on different substrates. $\phi_B = 45°$ and $\phi_E = 0°$. c) ξ_{FMR} from 5 to 9 GHz with the microwave direction $\phi_E = 0°$. d) Dependence of ξ_{FMR} on ϕ_E measured at $\phi_B = 45°$. e) Dependence of ξ_{FMR} on the SrRuO$_3$ thickness in KTO/SrRuO$_3$/Py. The shaded regions in (c,e) indicate average values within 1 standard deviation (s.d.).

a rectifying voltage V_{mix} is measured when a microwave J_c is applied to the bilayer under external in-plane magnetic field B. V_{mix} has a symmetric component (V_{sym}) with the amplitude V_S and an antisymmetric component (V_{asy}) with the amplitude V_A. The merit of ST-FMR is its self-calibrating nature, which allows comparison of the relative change in damping-like SOT efficiency (ξ_{FMR}) using the ratio V_S/V_A

$$\xi_{FMR} = \frac{V_S}{V_A} \frac{e\mu_0 M_s d_{SRO} d_{Py}}{\hbar} \sqrt{1 + \frac{\mu_0 M_{eff}}{B_{res}}} \qquad (1)$$

Here, e is the electron charge, μ_0 is the permeability of free space, $\hbar$ is the reduced Planck constant, and B_{res} is the resonant field. The thicknesses of the two layers are d_{SRO} and d_{Py}, respectively. The saturation magnetization and the effective in-plane magnetization of the Py layer are M_s and M_{eff}, respectively.

Typical spectra of V_{mix} and its components measured at 7 GHz with field direction $\phi_B = 45°$ are shown in Figure 2b. An obvious symmetric component is observed for SrRuO$_3$/Py deposited on both KTO and STO substrates, which indicates a substantial amount of damping-like SOT. By contrast, the

symmetric component is negligibly small for SrRuO$_3$/Py on NGO, which corresponds to a much smaller damping-like SOT. Figure 2c shows the ξ_{FMR} measured at different frequencies. The average ξ_{FMR} across the frequency range for SrRuO$_3$/Py on the KTO, STO, and NGO substrates are 0.154, 0.139, and 0.015, respectively. The values of ξ_{FMR} for the bilayers deposited on KTO and STO are similar to that for the orthorhombic SrRuO$_3$/Co bilayer measured by ST-FMR.[36] We verify that the variations in ξ_{FMR} across three substrates are not likely to be caused by differences in the longitudinal electrical resistivity ρ_{xx} of the SrRuO$_3$ layers, which are 174.7 μΩ cm (KTO), 120.5 μΩ cm (STO), and 114.3 μΩ cm (NGO), respectively (see Note S2, Supporting Information).

We modify parameters of our ST-FMR measurement to further investigate the physical significance of the observed ξ_{FMR}. In Figure 2d, ξ_{FMR} appears to be roughly independent of the microwave direction (ϕ_E) relative to the SrRuO$_3$ lattice for all three substrates. This implies that the intrinsic spin Hall conductivities of SrRuO$_3$ in all its three phases are more or less isotropic, as opposed to SrIrO$_3$.[15,37,38] Another possibility is the twinned crystal domains, which has been reported frequently

**ADVANCED
SCIENCE NEWS**
www.advancedsciencenews.com

**ADVANCED
MATERIALS**
www.advmat.de

in SrRuO$_3$[36,42] and other materials.[9] This would flatten the in-plane anisotropy of SOT in measurement, even it exists intrinsically. It has been reported that the measured SOT efficiencies are affected by many thickness-dependent mechanisms, such as spin diffusion length,[8] electrical resistivity,[31] and crystal phase.[36,38] We find that the thickness of the SrRuO$_3$ layer in this study is sufficiently large to have a notable effect on ξ_{FMR}. As seen from Figure 2e, there is almost no change in ξ_{FMR} when SrRuO$_3$ thickness in KTO/SrRuO$_3$/Py is reduced from 20 to 10 nm. This is consistent with the previous reports[36,38] and therefore we expect the crystal structure of SrRuO$_3$ to remain unchanged for both film thicknesses investigated here. Also, for SrRuO$_3$ film thickness of 10 nm and above, the electrical resistivity [31] and spin diffusion length[8] should be saturated. In addition, we measure the V_{mix} at varying external field direction ϕ_B, which is shown in Note S3 of the Supporting Information. Both V_{sym} and V_{asy} have only the $\sin(2\phi_B)\cos(\phi_B)$ component, suggesting the regular in-plane damping-like and out-of-plane field-like SOT. The only magnetic anisotropy in our SrRuO$_3$/Py samples is a small ($\approx$1.5 mT) in-plane uniaxial anisotropic field, which is consistent with the previous report on Py.[43]

The SOT efficiency extracted by the ratio analysis represents the relative strength of in-plane damping-like torque to out-of-plane field-like torque, where the latter has been assumed to be of a predominant Oersted origin in metals.[3,6,7] However, it is unclear if this assumption holds for oxides. We conduct two experiments to address this question. First, we measure the dampinglike SOT efficiency $\xi_{DL,\,FMR}$ using the DC-tuned ST-FMR technique (Note S4, Supporting Information). The results suggest that the SOT generated by SrRuO$_3$ is predominantly damping-like. Second, we use the in-plane HHV technique[12,44–46] to measure the SOT efficiency in SrRuO$_3$ (20 nm)/Py (4 nm) independently, where the SOT efficiency is extracted from the damping-like torque only (see the Experimental Section; Note S5 of the Supporting Information for details). **Figure 3**a shows a schematic setup of the HHV measurement. The second harmonic Hall resistance $R_{xy}^{2\omega}$ in response to an alternating current $J_c\sin(\omega t)$ is measured while an in-plane external magnetic field B applied at an angle ϕ_B with J_c. The measured $R_{xy}^{2\omega}$ is fitted against ϕ_B using

$$R_{xy}^{2\omega} = \frac{R_{PHE}\tau_{FL}}{\gamma B}\cos(2\phi_B)\cos(\phi_B)$$
$$+\left[\frac{R_{AHE}\tau_{DL}}{2\gamma(B+\mu_0 M_{eff})} + R_{ANE}\right]\cos(\phi_B) + R_x\sin(2\phi_B) \quad (2)$$

Here R_{PHE}, R_{AHE}, and γ are the planar Hall resistance, the anomalous Hall resistance, and the gyromagnetic ratio, respectively. The $\cos(2\phi_B)\cos(\phi_B)$ term describes the strength of field-like SOT (τ_{FL}). The $\cos(\phi_B)$ term consists of contributions from both the damping-like torque (τ_{DL}) and the anomalous Nernst effect (R_{ANE}). The $\sin(2\phi_B)$ term with amplitude R_x, which has been removed during data processing or sometimes ignored in previous studies, is likely to arise from a thermal gradient along the direction of current[45] (Note S6, Supporting Information). Figure 3b shows the typical $R_{xy}^{2\omega}$, which can be well fitted using Equation (2). After removing the constants from the amplitude of the $\cos(\phi_B)$ term, we plot $\frac{\tau_{DL}}{B+\mu_0 M_{eff}}$ against $\frac{1}{B+\mu_0 M_{eff}}$ to

extract the τ_{DL} from the gradient of the linear fit. In Figure 3c, the good linear relation for both devices on KTO and STO is the direct evidence of a sizable damping-like SOT at room temperature (300 K). On the other hand, the same plot for a device on NGO is rather scattered in a small range of $\frac{\tau_{DL}}{B+\mu_0 M_{eff}}$ across the same span of $\frac{1}{B+\mu_0 M_{eff}}$ as those on KTO and STO. This indicates that a negligible damping-like SOT is generated from NGO/SrRuO$_3$. The damping-like SOT efficiency can be computed using $\xi_{DL,HHV} = \frac{2e\tau_{DL}M_s d_{Py}}{\hbar\gamma J_{SRO}}$,[45] where J_{SRO} is the current density in the SrRuO$_3$ layer. We find $\xi_{DL,HHV}$ = 0.078, 0.035, and 0.008 at room temperature for SrRuO$_3$/Py KTO, STO, and NGO, respectively. This is consistent with the order of magnitude of ξ_{FMR}. The numerical discrepancies between $\xi_{DL,HHV}$ and ξ_{FMR} for the same sample are not fully understood at this stage, but have been prevalent in the previous studies as well.[45,47] The possible contributing factors are discussed in Note S7 of the Supporting Information. In Note S8 of the Supporting Information, we also evaluate that the observed differences in $\xi_{DL,HHV}$ and ξ_{FMR} across substrates are less likely to arise from the interface of SrRuO$_3$/Py, though oxidation of Py[48] might influence the interfacial transparency[36,49] of SrRuO$_3$/Py.

In order to interpret the origin of SOT generated by SrRuO$_3$, we examine the temperature (T) dependence of $\xi_{DL,HHV}$. The lowest temperature we present here is 180 K, which is sufficiently higher than the Curie temperature of all phases of SrRuO$_3$.[18,37,40] This ensures that magnetic moments contributing to the HHV measurement are predominantly from Py. Otherwise, the magnetic moments of ferromagnetic SrRuO$_3$ would complicate the signal and physical significance through mechanisms like magnetic inhomogeneity and spin-dependent scattering. In Figure 3d, both the $\xi_{DL,HHV}$ measured from KTO/SrRuO$_3$/Py and STO/SrRuO$_3$/Py are sizable and increase with decreasing T whereas the $\xi_{DL,HHV}$ for the case of NGO/SrRuO$_3$/Py is negligibly small and is almost independent of T. Assuming a spin Hall effect dominated SOT, we compute the effective SHC $\sigma_s = \frac{\xi_{DL,HHV}}{\rho_{xx}}$. Figure 3e summarizes the dependence of σ_s on both T and longitudinal electrical conductivity (σ_{xx}). σ_s shares the similar trend as $\xi_{DL,HHV}$ and its relative strength across substrates does not change with T. Since σ_s of SrRuO$_3$ deposited on both KTO and STO decreases rapidly with increasing T and decreasing σ_{xx}, it closely resembles the intrinsic SHC in the "dirty metal" regime.[36,39] In this scenario, the intrinsic contribution dominates the SHC and it decreases quickly with decreasing carrier mean lifetime τ, which can be gauged by measuring σ_{xx} since $\sigma_{xx} \propto \tau$.

Combining the results from ST-FMR and HHV measurements, we obtain the following implications. First, the SOT generated by SrRuO$_3$ is heavily influenced by its crystal structure, where KTO/SrRuO$_3$ produces the largest amount of SOT followed by STO/SrRuO$_3$, but NGO/SrRuO$_3$ produces negligible SOT. Second, the SOT is likely to arise from the intrinsic mechanism (Figure 3e) with a bulk-like behavior (Figure 2e). In an attempt to understand how the crystal structure of SrRuO$_3$ could possibly affect its SOT, we determine the type of octahedral rotation in different phases by examining half-integer

peaks from XRD measurement.[18,40,50] A vector $g*$ in the recip-rocal space of unit vector $a*$, $b*$, and $c*$ can be expressed as $g* = Ha* + Kb* + Lc*$. The half-integer measurements are per-formed in the coordinate system of the substrates with fixed H and K values but varying L, which we refer as L scan here. **Figure 4**a shows the L scans along selected directions for NGO/SrRuO₃. The absence of the (0, 1/2, L) film peaks implies the absence of a^+ rotation. The absence of the (1/2, 1/2, L) film peaks implies the absence of a^-, b^-, and c^+ rotations. The pres-ence of the (1/2, 3/2, 3/2) peak implied the presence of either b^- or c^- rotation. Therefore, the combined results from Figure 4a imply that the octahedral rotation for SrRuO₃ on NGO is $a^0a^0c^-$. Here, "a", "b", and "c" denote the axis of rotation; "+", "−", and "0" on the superscript indicate in-phase, out-of-phase, and no

octahedral rotation, respectively. In Figure 4b, the presence of the (0, 1/2, 2) peak indicates the presence of b^+ rotation, which also excludes the b^- rotation. The presence of the (1/2, 1/2, 3/2) peak suggests the presence of either a^- or b^- rotation. The pres-ence of the (1/2, 3/2, 3/2) peak indicates either b^- or c^-. There-fore, the octahedral rotation of SrRuO₃ on STO substrate is $a^-b^+c^-$. In Figure 4c, similar to the other two substrates, it can be shown that either a^-, b^- or c^- and/or the combination of them is present. Considering the present film peaks are consistent with the previous studies[18,51] and the allowed space group, the octa-hedral rotation of SrRuO₃ on KTO is determined to be $a^-a^-c^+$. Note that this type of octahedral rotation can also be labeled as $a^+c^-c^-$, depending on the orientation of the c-axis of the orthorhombic lattice.[42,51] The combined results of the lattice
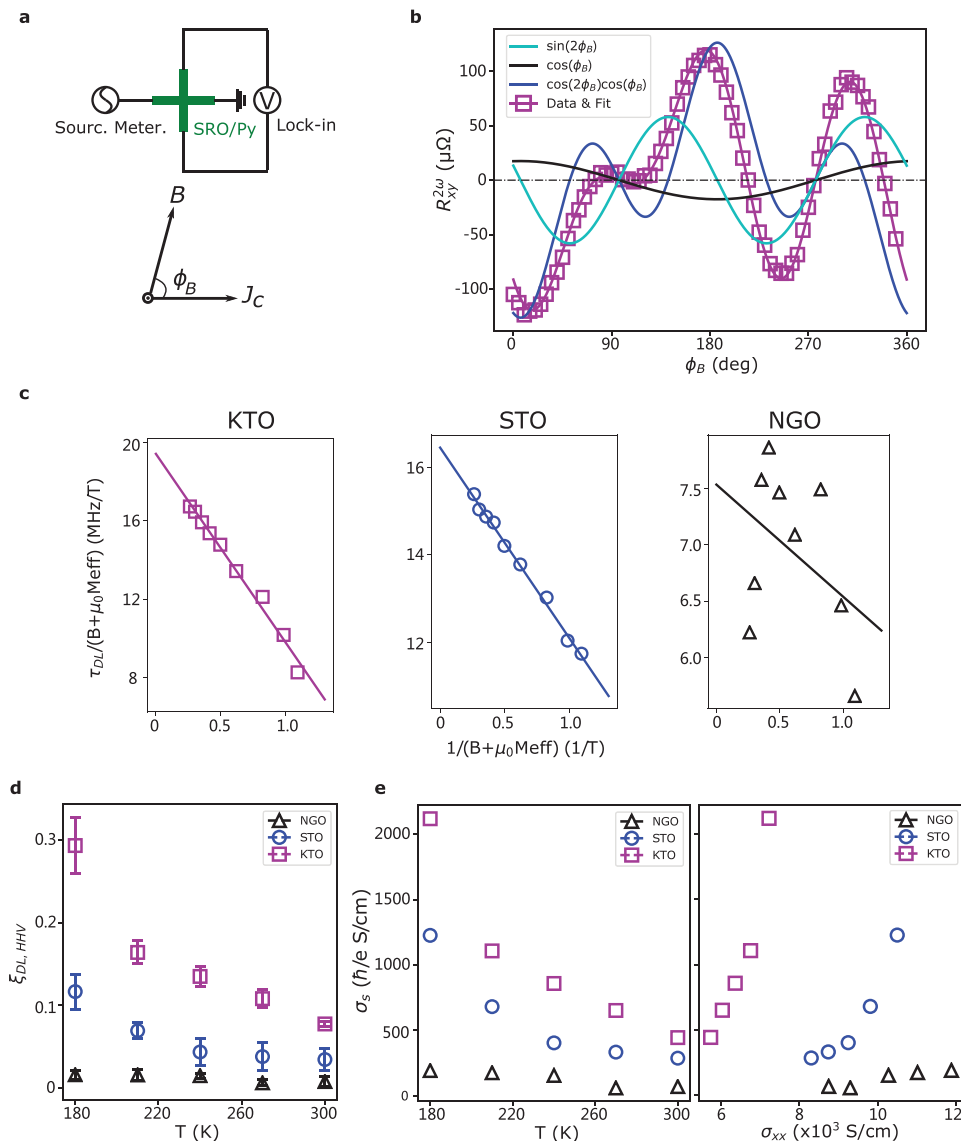

Figure 3. SOT evaluated by HHV technique. a) Schematic setup. b) Typical second harmonic Hall resistance ($R_{xy}^{2\omega}$) at J_c = 8 mA and B = 0.1 T using NGO/SrRuO₃/Py at room temperature. c) Linear plot of $\frac{\tau_{DL}}{B+\mu_0 M_{eff}}$ against $\frac{1}{B+\mu_0 M_{eff}}$ for SrRuO₃/Py deposited on different substrates. d) Extracted SOT efficiency ($\xi_{DL, HHV}$) at different temperature (T). e) Dependence of effective SHC (σ_s) on T (left) and longitudinal electrical conductivity (σ_{xx}) (right).

**ADVANCED
SCIENCE NEWS**

www.advancedsciencenews.com
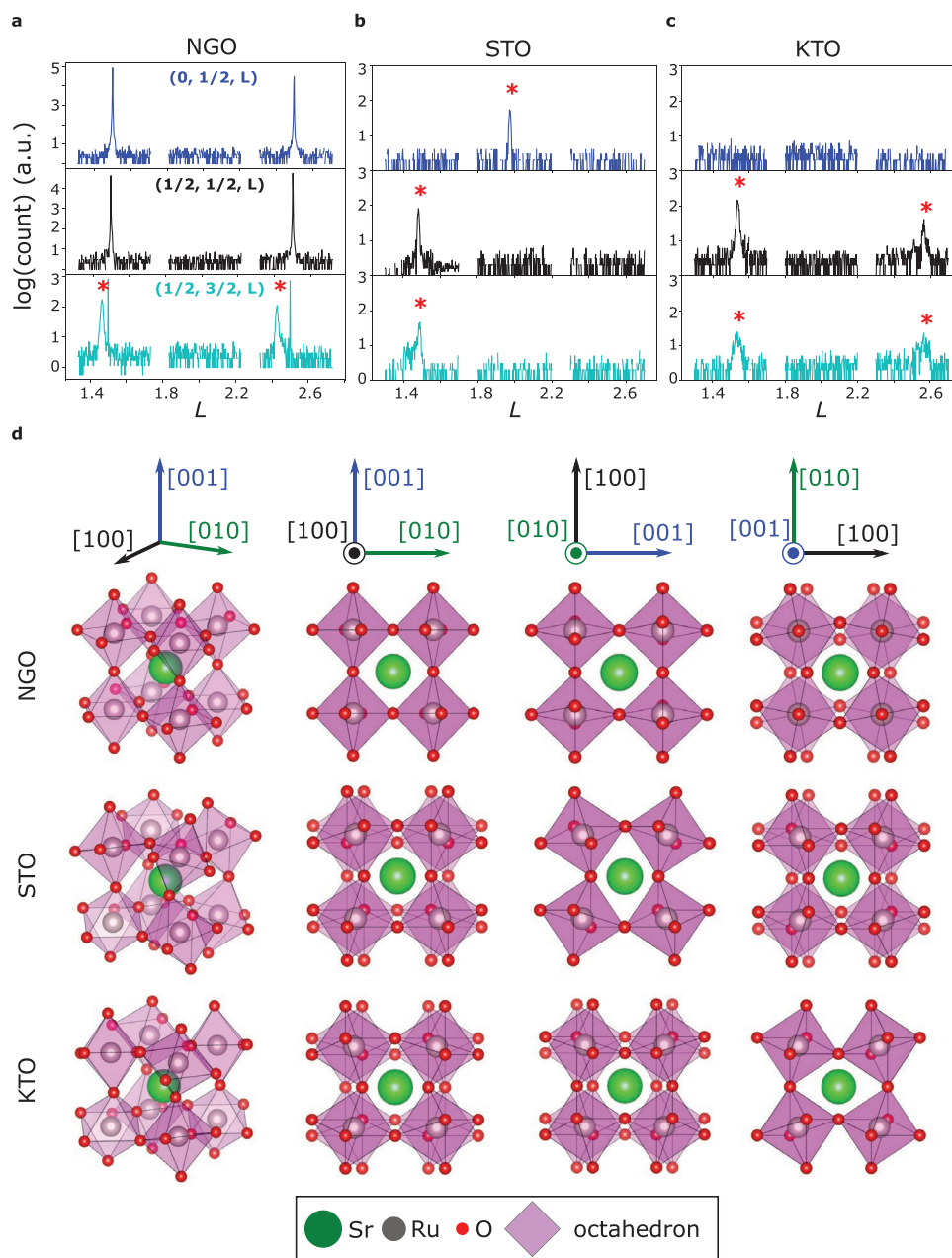
**ADVANCED
MATERIALS**

www.advmat.de

Figure 4. Octahedral rotation in SrRuO₃ of different crystal structures. a–c) *L* scans along selected directions for SrRuO₃ deposited on different substrates. Film peaks are indicated by "*". The six sharp and narrow peaks in (a) arise from the NGO substrate. The measurement coordinates are defined with reference to the lattice of the substrates. d) Octahedral rotation in SrRuO₃ deposited on KTO, STO, and NGO substrate. Coordinates are defined with reference to the pseudocubic lattice of SrRuO₃.

parameters and the types of octahedral rotation also allow us to determine the crystal structure SrRuO₃. Our SrRuO₃ thin films are tetragonal, monoclinic, and orthorhombic when deposited on NGO, STO, and KTO substrates, respectively (Note S9, Supporting Information).

The types of octahedral rotation in SrRuO₃ on each substrate are schematically shown in Figure 4d. We find that the SrRuO₃ thin film has no octahedral rotation (a^0) around the in-plane axes when depositing on NGO, where minimum SOT efficiencies (ξ_{FMR} and $\xi_{DL,HHV}$) are observed. By contrast, relatively

larger SOT efficiencies are correlated to the presence of both in-phase (b^+) and out-of-phase (a^-) octahedral rotations around the in-plane axes of SrRuO₃ deposited on STO and KTO substrates. This is consistent with the previous theoretical studies.[15,30] It has been predicted[30] that in a transition metal oxide like SrRuO₃, the distortion of the octahedral crystal field due to octahedral rotation splits the e_g and t_{2g} manifolds into sub-bands, where an overlap between the manifolds or sub-bands is supported by the effect of spin–orbit coupling. This counters the dampening effect of a strong crystal field on the spin Hall

effect and results in substantially enhanced intrinsic SHC. In our study, owning to the smallest lattice mismatch between STO and SrRuO$_3$, an intermediate crystal structure of SrRuO$_3$ is produced, where an intermediate octahedral rotation is also expected. It is therefore not surprising that the SOT efficiency of SrRuO$_3$ deposited on STO is always between those from the other two substrates, regardless of the measurement method.

To verify the effect of octahedral rotations, we perform first-principles calculations on the intrinsic SHC in bulk SrRuO$_3$ under different strain conditions (see Note S10, Supporting Information). Using the same type of octahedral rotations and the same lattice parameters as experimentally found, we calculate the values of SHC for SrRuO$_3$ on KTO and STO substrates to be much larger than the value of SHC for SrRuO$_3$ on NGO substrate (Figure S9a, Supporting Information). In Figure S11 of the Supporting Information, we show that the calculated intrinsic spin Hall conductivity increases with the angle of octahedral rotation. These results are consistent with our experimental observations indicating that the type and magnitude of the octahedral rotation in SrRuO$_3$ plays a decisive role in controlling the SHC. While changes in the lattice volume also affect the SHC (Figure S10, Supporting Information), they solely cannot explain the experimentally observed SOT efficiencies.

In summary, we have investigated the SOT efficiencies of perovskite oxide SrRuO$_3$ in three crystal structures determined by epitaxial growth of SrRuO$_3$ thin films on different substrates. Using two complementary techniques, spin-torque ferromagnetic resonance and in-plane harmonic Hall voltage measurements, we find that the measured SOT efficiencies of the SrRuO$_3$/Py bilayer deposited on KTO, STO, and NGO substrates at room temperature are $\xi_{FMR} = 0.154$, 0.139, and 0.015, and $\xi_{DL,HHV} = 0.078$, 0.035, and 0.008, respectively. The relative strength of $\xi_{DL,HHV}$ does not change when lowering the temperature to 180 K. Dependence of the σ_s on T and σ_{xx} suggests that the dominant contribution to the SOT generated by SrRuO$_3$ is the intrinsic SHC in the "dirty metal" regime. By examining the types of octahedral rotation, we find that the strength of SOT in SrRuO$_3$ is strongly correlated to the octahedral rotation around its in-plane axes.

Experimental Section

Sample Fabrication: The SrRuO$_3$ layer was deposited using a pulsed laser deposition system at 750 °C and under an oxygen pressure of 150 mTorr. They were cooled down to room temperature before transferring in situ to an interconnected sputtering chamber. Then the Py layer was deposited at room temperature using DC magnetron sputtering method with a base pressure of less than 2×10^{-8} Torr. All samples were passivated by a 2 nm SiO$_2$ layer using RF magnetron sputtering. The SrRuO$_3$/Py bilayer was patterned into microstrip and 6-terminal Hall bar devices by the combination of photolithography and ion beam etching. The microstrip device for ST-FMR measurement has a dimension of 10 μm × 40 μm. The Hall bar device has a width of 10 μm and Hall lead width of 5 and 40 μm between Hall leads. Both types of devices are terminated by a thick electrode of Ti (5 nm)/Cu (100 nm).

Structural Characterization: All of the X-ray diffraction measurements were performed at room temperature at the Singapore Synchrotron Light Source with an X-ray wavelength of 1.541 Å (Cu K$_\alpha$ radiation).

Measurement of SOT: A Rohde & Schwarz SMB 100A signal generator was used to provide the modulated microwave for ST-FMR

measurement. The microwave has the frequency of 5–9 GHz, a modulation frequency of 317.3 Hz and a nominal power of 18 dBm. The rectifying voltage was collected using a Zurich Instrument MFLI lock-in amplifier. A Keithley 6221 source meter was used to generate AC current of 317.3 Hz for the HHV measurement. The current amplitude for the data in the main text is 8 mA, which is equivalent to 3.3×10^6 A cm^{-2}. The first and second harmonic Hall voltages were collected using the same lock-in amplifier above.

Supporting Information

Supporting Information is available from the Wiley Online Library or from the author.

Conflict of Interest

The authors declare no conflict of interest.

Data Availability Statement

The data that support the findings of this study are available from the corresponding author upon reasonable request.

[1] A. Manchon, J. Železný, I. M. Miron, T. Jungwirth, J. Sinova, A. Thiaville, K. Garello, P. Gambardella, *Rev. Mod. Phys.* **2019**, *91*, 035004.

[2] A. Manchon, S. Zhang, *Phys. Rev. B* **2008**, *78*, 212405.

[3] L. Liu, T. Moriyama, D. C. Ralph, R. A. Buhrman, *Phys. Rev. Lett.* **2011**, *106*, 036601.

[4] D. Fang, H. Kurebayashi, J. Wunderlich, K. Vyborny, L. P. Zarbo, R. P. Campion, A. Casiraghi, B. L. Gallagher, T. Jungwirth, A. J. Ferguson, *Nat. Nanotechnol.* **2011**, *6*, 413.

[5] M. O. A. Chernyshov, X. Liu, J. K. Furdyna, Y. Lyanda-Geller, L. P. Rokhinson, *Nat. Phys.* **2009**, *5*, 656.

[6] L. Liu, C.-F. Pai, Y. Li, H. W. Tseng, D. C. Ralph, R. A. Buhrman, *Science* **2012**, *336*, 555.

[7] C. Pai, L. Liu, Y. Li, H. W. Tseng, D. C. Ralph, R. A. Buhrman, *Appl. Phys. Lett.* **2012**, *101*, 122404.

[8] W. Zhang, M. B. Jungfleisch, W. Jiang, J. E. Pearson, A. Hoffmann, F. Freimuth, Y. Mokrousov, *Phys. Rev. Lett.* **2014**, *113*, 196602.

**ADVANCED
SCIENCE NEWS**

www.advancedsciencenews.com

**ADVANCED
MATERIALS**

www.advmat.de

[9] J. Zhou, X. Wang, Y. Liu, J. Yu, H. Fu, L. Liu, S. Chen, J. Deng, W. Lin, X. Shu, H. Y. Yoong, T. Hong, M. Matsuda, P. Yang, S. Adams, B. Yan, X. Han, J. S. Chen, *Sci. Adv.* **2019**, *5*, 6696.

[10] Y. Fan, P. Upadhyaya, X. Kou, M. Lang, S. Takei, Z. Wang, J. Tang, L. He, L. Chang, M. Montazeri, G. Yu, W. Jiang, T. Nie, R. N. Schwartz, Y. Tserkovnyak, K. L. Wang, *Nat. Mater.* **2014**, *13*, 699.

[11] A. R. Mellnik, J. S. Lee, A. Richardella, J. L. Grab, P. J. Mintun, M. H. Fischer, A. Vaezi, A. Manchon, E.-A. Kim, N. Samarth, D. C. Ralph, *Nature* **2014**, *511*, 449.

[12] D. MacNeill, G. M. Stiehl, M. H. D. Guimaraes, R. A. Buhrman, J. Park, D. C. Ralph, *Nat. Phys.* **2017**, *13*, 300.

[13] M. H. D. Guimarães, G. M. Stiehl, D. MacNeill, N. D. Reynolds, D. C. Ralph, *Nano Lett.* **2018**, *18*, 1311.

[14] Q. Xie, W. Lin, B. Yang, X. Shu, S. Chen, L. Liu, X. Yu, M. B. H. Breese, T. Zhou, M. Yang, Z. Zhang, S. Wang, H. Yang, J. Chai, X. Han, J. Chen, *Adv. Mater.* **2019**, *31*, 1900776.

[15] A. S. Patri, K. Hwang, H. Lee, Y. B. Kim, *Sci. Rep.* **2018**, *8*, 8052.

[16] Z. Fang, N. Nagaosa, K. S. Takahashi, A. Asamitsu, R. Mathieu, T. Ogasawara, H. Yamada, M. Kawasaki, Y. Tokura, K. Terakura, *Science* **2003**, *302*, 92.

[17] R. Mathieu, A. Asamitsu, H. Yamada, K. S. Takahashi, M. Kawasaki, Z. Fang, N. Nagaosa, Y. Tokura, *Phys. Rev. Lett.* **2004**, *93*, 016602.

[18] W. Lu, W. Song, P. Yang, J. Ding, G. M. Chow, J. S. Chen, *Sci. Rep.* **2015**, *5*, 10245.

[19] A. Grutter, E. A. F. Wong, M. Liberati, A. Vailionis, Y. Suzuki, *Appl. Phys. Lett.* **2010**, *96*, 082509.

[20] M. Ziese, I. Vrejoiu, D. Hesse, *Phys. Rev. B* **2010**, *81*, 184418.

[21] Q. Gan, R. A. Rao, C. B. Eom, J. L. Garrett, M. Lee, *Appl. Phys. Lett.* **1998**, *72*, 978.

[22] A. T. Zayak, X. Huang, J. B. Neaton, K. M. Rabe, *Phys. Rev. B* **2008**, *77*, 214410.

[23] A. Herklotz, M. Kataja, K. Nenkov, M. D. Biegalski, H.-M. Christen, C. Deneke, L. Schultz, K. Doerr, *Phys. Rev. B* **2013**, *88*, 144412.

[24] S. Lin, Q. Zhang, M. A. Roldan, S. Das, T. Charlton, M. R. Fitzsimmons, Q. Jin, S. Li, Z. Wu, S. Chen, H. Guo, X. Tong, M. He, C. Ge, C. Wang, L. Gu, K. Jin, E. Guo, *Phys. Rev. Appl.* **2020**, *13*, 034033.

[25] W. Lu, W. D. Song, K. He, J. Chai, C. Sun, G. Chow, J. Chen, *J. Appl. Phys.* **2013**, *113*, 063901.

[26] Q. Qin, W. Song, S. He, P. Yang, J. Chen, *J. Phys. D: Appl. Phys.* **2017**, *50*, 215002.

[27] M. C. Langner, C. L. S. Kantner, Y. H. Chu, L. M. Martin, P. Yu, J. Seidel, R. Ramesh, J. Orenstein, *Phys. Rev. Lett.* **2009**, *102*, 177601.

[28] G. Koster, L. Klein, W. Siemons, G. Rijnders, J. S. Dodge, C. B. Eom, D. H. A. Blank, M. R. Beasley, *Rev. Mod. Phys.* **2012**, *84*, 253.

[29] M. W. Haverkort, I. S. Elfimov, L. H. Tjeng, G. A. Sawatzky, A. Damascelli, *Phys. Rev. Lett.* **2008**, *101*, 026406.

[30] P. Jadaun, L. F. Register, S. K. Banerje, *Proc. Natl. Acad. Sci. USA* **2020**, *117*, 11878.

[31] J. Zhou, X. Shu, Y. Liu, X. Wang, W. Lin, S. Chen, L. Liu, Q. Xie, T. Hong, P. Yang, B. Yan, X. Han, J. Chen, *Phys. Rev. B* **2020**, *101*, 184403.

[32] L. Hao, D. Meyers, H. Suwa, J. Yang, C. Frederick, T. R. Dasa, G. Fabbris, L. Horak, D. Kriegner, Y. Choi, J.-W. Kim, D. Haskel, P. J. Ryan, H. Xu, C. D. Batista, M. P. M. Dean, J. Liu, *Nat. Phys.* **2018**, *14*, 806.

[33] L. Chen, C. Xu, H. Tian, H. Xiang, J. Íñiguez, Y. Yang, L. Bellaiche, *Phys. Rev. Lett.* **2019**, *122*, 247701.

[34] D. Yi, Y. Wang, O. M. J. van't Erve, L. Xu, H. Yuan, M. J. Veit, P. P. Balakrishnan, Y. Choi, A. T. N'Diaye, P. Shafer, E. Arenholz, A. Grutter, H. Xu, P. Yu, B. T. Jonker, Y. Suzuki, *Nat. Commun.* **2020**, *11*, 902.

[35] M. S. Saleem, B. Cui, C. Song, Y. Sun, Y. Gu, R. Zhang, M. U. Fayaz, X. Zhou, P. Werner, S. S. P. Parkin, F. Pan, *ACS Appl. Mater. Interfaces* **2019**, *11*, 6581.

[36] Y. Ou, Z. Wang, C. S. Chang, H. P. Nair, H. Paik, N. Reynolds, D. C. RalphDavid, A. MullerDarrell, G. SchlomRobert, A. Buhrman, *Nano Lett.* **2019**, *19*, 3663.

[37] L. Liu, Q. Qin, W. Lin, C. Li, Q. Xie, S. He, X. Shu, C. Zhou, Z. Lim, J. Yu, W. Lu, M. Li, X. Yan, S. J. Pennycook, J. Chen, *Nat. Nanotechnol.* **2019**, *14*, 939.

[38] T. Nan, T. J. Anderson, J. Gibbons, K. Hwang, N. Campbell, H. Zhou, Y. Q. Dong, G. Y. Kim, D. F. Shao, T. R. Paudel, N. Reynolds, X. J. Wang, N. X. Sun, E. Y. Tsymbal, S. Y. Choi, M. S. Rzchowski, Y. B. Kim, D. C. Ralph, C. B. Eom, *Proc. Natl. Acad. Sci. USA* **2019**, *116*, 16186.

[39] L. Zhu, L. Zhu, M. Sui, D. C. Ralph1, R. A. Buhrman, *Sci. Adv.* **2019**, *5*, 8025.

[40] W. Lu, Y. P. Yang, W. D. Song, G. M. Chow, J. S. Chen, *Phys. Rev. B* **2013**, *88*, 214115.

[41] P. Yang, H. Liu, Z. Chen, L. Chen, J. Wang, *J. Appl. Crystallogr.* **2014**, *47*, 402.

[42] A. F. Marshall, L. Klein, J. S. Dodge, C. H. Ahn, J. W. Reiner, L. Mieville, L. Antagonazza, A. Kapitulnik, T. H. Geballe, M. R. Beasley, *J. Appl. Phys.* **1999**, *85*, 4131.

[43] V. Tshitoyan, C. Ciccarelli, A. P. Mihai, M. Ali, A. C. Irvine, T. A. Moore, T. Jungwirth, A. J. Ferguson, *Phys. Rev. B* **2015**, *92*, 214406.

[44] C. O. Avci, K. Garello, M. Gabureac, A. Ghosh, A. Fuhrer, S. F. Alvarado, P. Gambardella, *Phys. Rev. B* **2014**, *90*, 224427.

[45] S. Karimeddiny, J. A. Mittelstaedt, R. A. Buhrman, D. C. Ralph, *Phys. Rev. Appl.* **2020**, *14*, 024024.

[46] R. Itoh, Y. Takeuchi, S. DuttaGupta, S. Fukami, H. Ohno, *Appl. Phys. Lett.* **2019**, *115*, 242404.

[47] C.-F. Pai, Y. Ou, L. H. Vilela-Leão, D. C. Ralph, R. A. Buhrman, *Phys. Rev. B* **2015**, *92*, 064426.

[48] A. Bose, J. N. Nelson, X. S. Zhang, P. Jadaun, R. Jain, D. G. Schlom, D. C. Ralph, D. A. Muller, K. M. Shen, R. A. Buhrman, *ACS Appl. Mater. Interfaces* **2020**, *12*, 55411.

[49] W. Zhang, W. Han, X. Jiang, S.-H. Yang, S. S. P. Parkin, *Nat. Phys.* **2015**, *11*, 496.

[50] D. I. Woodward, I. M. Reaney, *Acta Crystallogr., Sect. B: Struct. Sci.* **2005**, *61*, 387.

[51] B. J. Kennedy, B. A. Hunter, *Phys. Rev. B* **1998**, *58*, 653.